

## Shell-specific Interpolation of Measured 3D Displacements, for Micromechanics-Based Rapid Safety Assessment of Shotcrete Tunnels

S. Ullah<sup>1</sup>, B. Pichler<sup>1</sup>, S. Scheiner<sup>1,2</sup>, and C. Hellmich<sup>1,3</sup>

**Abstract:** Point-wise optical measurements of 3D displacement vectors over time are a key input for monitoring shotcrete tunnel shells during construction according to the New Austrian Tunnelling Method (NATM). Aiming at estimation of the stresses prevailing in the highly loaded, hydrating material, we here deal with two different interpolation strategies for reconstructing, from measured displacement vectors, the 3D displacement field histories of the inner surface of the tunnel shell. The first approach considers spatial interpolation of displacement components in a fixed Cartesian base frame, while the second (new) approach refers to displacement components in a moving base frame consisting of vectors tangent to the cylindrical coordinate curves along the tunnel shell. Subsequently, thin shell kinematics allow for (analytical) conversion of the aforementioned displacement field histories into strain field histories throughout the entire tunnel shell. Finally, thermochemomechanical constitutive modeling (including extension of a recently developed, experimentally validated micro-viscoelasticity model for hydrating shotcrete, towards the nonlinear regime) allows for conversion of the aforementioned strain fields into stress fields. The latter differ qualitatively, depending on the chosen interpolation strategy. Thereby, the moving base frame-related interpolation scheme results in more realistic estimations of the actual load carrying behavior of an NATM tunnel.

**Keywords:** NATM, monitoring, displacement, interpolation, micromechanics, shell theory, shotcrete, hydration.

---

<sup>1</sup> Institute for Mechanics of Materials and Structures, Vienna University of Technology, Karlsplatz 13/202, A-1040 Vienna, Austria

<sup>2</sup> Current address: School of Computer Science and Software Engineering, The University of Western Australia, 35 Stirling Highway, Crawley WA 6009, Australia

<sup>3</sup> Corresponding author, Associate Professor, Institute for Mechanics of Materials and Structures, Vienna University of Technology, Karlsplatz 13/202, A-1040, Vienna, Austria. Tel.: +43-1-58801-20220; Fax: +43-1-58801-20299; E-mail: Christian.Hellmich@tuwien.ac.at

## 1 Introduction

The New Austrian Tunnelling Method (NATM) is a very flexible mode of tunnel construction. The method, pioneered by Rabcewicz [Rabcewicz (1948)], can be easily adopted to variations in geological properties of the ground and to changes in size and curvature of the tunnel. When driving tunnels according to the NATM, shotcrete is applied onto the freshly excavated stretch in form of a thin shell. The lining is produced either in a single step (full face excavation) or in a series of subsequent steps, e.g. starting with the top heading, followed by the benches, and completed by the invert (sequential excavation).

The NATM concept is based on mastering the interaction between the viscous ground and the installed, rather flexible, and aging shotcrete tunnel shell. Consequently, hydrating characteristics of the shotcrete, creep characteristics of the ground and the time lapse between the excavation and shotcreting are key design parameters for the success of the NATM; e.g. too stiff shells or shells installed too early, trying to restrict stress redistribution in the ground after excavation, may be destroyed whereas too soft shells or shells put up too late may not be able to prevent loss of stability of the opening [Pacher (1964)].

Day-to-day on-site structural monitoring is the key tool by which NATM engineers reveal the interaction between the ground and the tunnel shell. Nowadays, laser optical systems for measuring 3D displacement vectors of the tunnel shell are the golden standard [Schubert and Steindorfer (1996); Steindorfer, Schubert, and Rabensteiner (1995)]. Based on these measurements it is decided whether or not additional ground support, by means of rock bolts, is installed to further promote stability of the opening. Moreover, these measurements allow for a qualitative prediction of the rock stiffness ahead of the tunnel face [Steindorfer and Schubert (1997)].

In addition to the rock stiffness changes, the forces and stresses in the tunnel shell are key quantities governing the safety of the tunnel driving process. These forces and stresses can be estimated from combination of the displacement measurement data with advanced material models for hydrating shotcrete, in the framework of so-called hybrid methods [Rokahr (1997); Hellmich, Macht, and Mang (1999); Hellmich, Mang, and Ulm (2001); Lackner, Macht, Hellmich, and Mang (2002); Macht, Lackner, Hellmich, and Mang (2003)]. In more detail, displacement fields are approximated from pointwisely measured displacement vectors, and these fields are prescribed as boundary values onto a structural model of the tunnel shell, such as a 3D Finite Element (FE) model. Corresponding structural computations require elaborate material models for shotcrete [Meschke (1996)], considering mechanical properties that evolve because of hydration [Hellmich and Mang (2005); Hellmich,

Mang, and Ulm (2001)]. The latter consideration can be naturally realized in the framework of continuum micromechanics [Zaoui (2002)] when, within a representative volume element (RVE) of shotcrete, the mechanical interaction of aggregates, cement, water, and of the reaction products of the latter two, called hydrates, are quantified, based on hydration-dependent, time-evolving volume fractions of the material constituents, which, at the same time, exhibit universal shotcrete-independent non-aging (i.e. constant) mechanical properties such as elastic properties [Hellmich and Mang (2005)], strength properties [Pichler, Hellmich, and Eberhardsteiner (2009); Pichler, Scheiner, and Hellmich (2008)], and creep properties [Scheiner and Hellmich (2009)].

While extending these latest achievements in multiscale modeling of shotcrete, the focus of the present paper is the mode of interpolation by which pointwisely measured displacement data are translated into spatial displacement fields. Corresponding interpolation schemes are realized for the Sieberg tunnel, shortly introduced in Section 2. Displacement components which are defined with respect to different base frames, are interpolated between the measurement points of this tunnel (Section 3). As to minimize computer time, we follow earlier examples relying on thin shell theory kinematics [Lackner, Macht, and Mang (2006); Macht, Lackner, Hellmich, and Mang (2003)]. However, in contrast to these earlier studies, we here employ an entirely analytical approach (Section 4). We then review the upscaling of shotcrete strength and extend multiscale shotcrete creep to the nonlinear loading regime (Section 5), before documenting the corresponding stresses in the Sieberg tunnel, estimated on the basis two different displacement interpolation schemes (Section 6), followed by Discussion (Section 7) and Conclusion (Section 8).

## 2 Excavation and monitoring of Sieberg tunnel

Our estimations of the stress state in a shotcrete tunnel shell are developed by example of a typical, widely employed type of geometry and measurement equipment used in NATM-tunneling, namely the measurement cross-section MC1452 of the Sieberg tunnel, constructed in the late 1990s as part of the high-capacity railway line Vienna-Salzburg, in Austria. Around measurement cross-section MC1452 (denoted as the *considered* measurement cross-section in the following), the Sieberg tunnel was driven through Miocene clay marl (with typical cohesion  $c = 0.01$  MPa, angle of internal friction  $\phi = 25^\circ$  [Rabcewicz (1969)], and unit weight  $\rho = 2600$  kg/m<sup>3</sup>) covered by meadow loam and Pleistocene gravels. The overburden depth was about 20 m [Poleschinski and Müller (1999)]. In addition, the water table was above the tunnel roof and the maximum water pressure was approximately 0.29 MPa [Maidl, Schmid, Ritz, and Herrenknecht (2008)]. Cross section MC1452 consists of cylindrical shell segments with piece-wise constant curvature, see Fig. 1 for

related geometrical dimensions. The latter are quantified through a right-handed

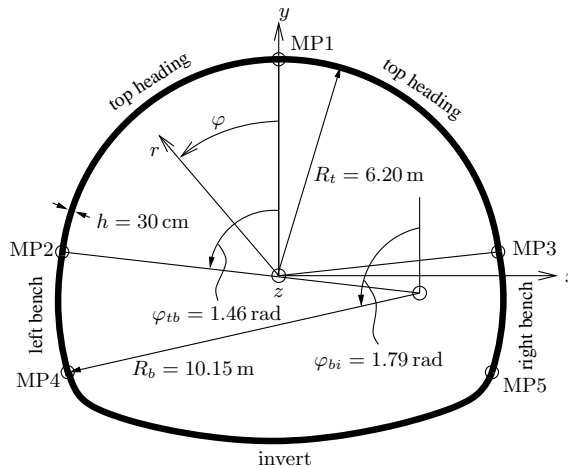


Figure 1: Considered cross-section of Sieberg tunnel constructed by sequential excavation according to the New Austrian Tunneling Method: definition of  $(x, y, z)$  and  $(r, \varphi, z)$  coordinate frames, structural dimensions, geometric properties and locations of measurement points (MPs)

Cartesian coordinate frame  $(x, y, z)$  (see Fig. 1), where the  $x$ -axis points into the horizontal direction, normal to the tunnel axis, which is aligned to the  $z$ -axis. In addition, we use a shell-intrinsic cylindrical base frame (defining coordinates  $r, \varphi, z$ ). Thereby,  $r$  denotes the radial distance to the (local) center of curvature of the cylindrical shell, and the angle  $\varphi$  (ranging from  $-\pi$  to  $+\pi$ ) describes the circumferential distance from the vertical plane containing the tunnel axis. In this sense,  $R_t = 6.20\text{ m}$  and  $R_b = 10.15\text{ m}$  denote the radii of curvature of the midsurfaces of the top heading and of the benches, respectively.  $+\varphi_{tb} = \varphi_2 = 1.46\text{ rad}$  and  $-\varphi_{tb} = \varphi_3 = -1.46\text{ rad}$  denote the positions of the interfaces between the top heading and the benches, while  $+\varphi_{bi} = \varphi_4 = 1.79\text{ rad}$  and  $-\varphi_{bi} = \varphi_5 = -1.79\text{ rad}$  denote the positions between the benches and the invert, respectively.

In the course of a sequential excavation strategy, the top heading at MC1452 was placed on Dec 14, 1997 (see Table 1 for a construction history of the investigated part of the Sieberg tunnel). Thereby, the rather poor ground conditions did not allow for a notable time lag between excavation and shotcreting, and rock bolts reinforced the interface between tunnel shell and surrounding ground [Ramspacher and Schwab (1998)]. >From Dec 14 to 22, tunnel advance by means of excavation of top heading was carried out. From Dec 19, when the tunnel face had reached a

Table 1: Construction history of Sieberg tunnel (sequential excavation)

Cross-section	Date of installation		
	Top heading	Left bench	Right bench
MC1444	Dec 12, 1997	Jan 18, 1998	Jan 20, 1998
MC1452	Dec 14, 1997	Jan 19, 1998	Jan 21, 1998
MC1462	Dec 16, 1997	Jan 26, 1998	Jan 22, 1998
MC1474	Dec 19, 1997	Jan 30, 1998	Jan 30, 1998
MC1483	Jan 09, 1998	Feb 02, 1998	Jan 31, 1998
MC1494	Jan 13, 1998	Feb 04, 1998	Feb 05, 1998
MC1502	Jan 16, 1998	Feb 09, 1998	Feb 06, 1998

distance of some 25 meters from the *considered* MC, to Jan 06, the tunnelling crew went on Christmas holidays. Top heading excavation work was resumed on Jan 07 such that on Jan 16 the tunnel face had reached a distance of around 50 meters from the *considered* MC. At that time, tunnel driving was ceased and further works were devoted to installation of benches, starting about 60 meters behind the face i.e. some 10 meters behind the *considered* MC. At this cross-section, the left bench was placed on Jan 19, 1998, and the right bench was placed on Jan 21, 1998. Until Feb 02, continued bench installation arrived at MC1494, i.e. 42 meters ahead of the *considered* MC. Placement of the invert and, hence, finalization of MC1452 was carried out several months later. Since the analysis described herein refers to the first 50 days after placement of the top heading, the invert will not be dealt with in the sequel of this paper.

For monitoring of 3D displacements in the *considered* MC, five measurement points (MPs) were installed: MP1, MP2, and MP3 at the crown, left foot, and right foot of the top heading; MP4 and MP5 at the footings of left bench and right bench, respectively (see Fig. 1). The same geometry and measurement equipment characterize the *preceding* measurement cross-section MC1444, installed 2 days prior to and 8 m distant from MC1452. For the subsequent analyses, we will consider displacement measurements collected at these two measurement cross sections between Dec 14, 1997, and Feb 2, 1998. Except for the Christmas break, during which monitoring intervals were enlarged due to the absence of excavation works, displacement measurements were taken at all installed MPs on a daily basis, in terms of Cartesian components related to the fixed  $(x,y,z)$ -system of Fig. 1, see Fig. 2 and Fig. 3 for the *considered* and *preceding* measurement cross-sections (MC1452 and MC1444), respectively. Based on the displacement measurements collected at

these two measurement cross-sections, we will reconstruct the displacement fields in this tunnel portion, as described next.

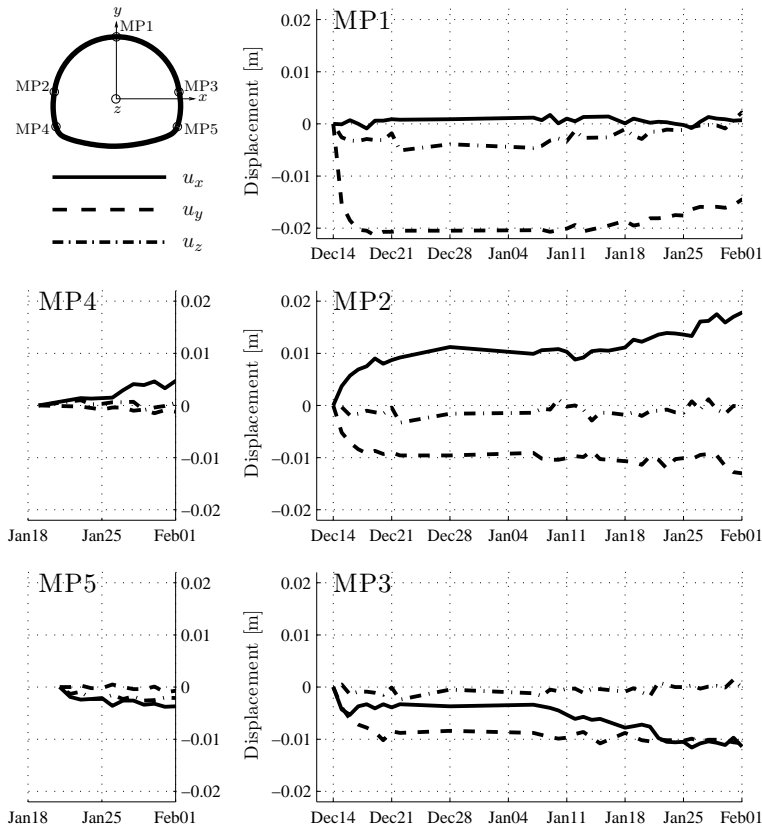


Figure 2: Histories of displacement components in  $x, y,$  and  $z$  directions measured at measurement points MP1 through MP5 of the *considered* measurement cross-section (MC1452)

### 3 Reconstructing the displacement fields of the tunnel shell: interpolation between measured 3D displacement vectors

Interpolation is used to construct continuous displacement functions providing a smooth transition between discrete displacement measurement data referring to different points in space and to different instants of time. Since displacement measurements are available in the form of 3D displacement vectors, three scalar quantities have to be interpolated, e.g. the length of the vectors and two angles defining their

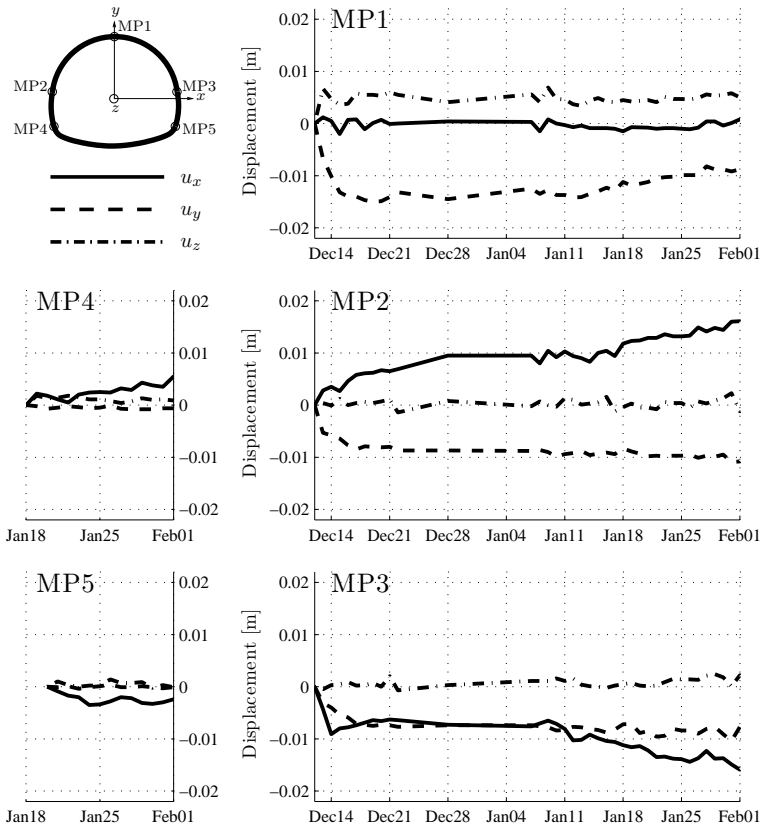


Figure 3: Histories of displacement components in  $x, y,$  and  $z$  directions measured at measurement points MP1 through MP5 of the *preceding* measurement cross-section (MC1444)

orientation in 3D Euclidean space or, alternatively, three vector components. This provides the motivation to deal with interpolation between scalar quantities  $q$ .

### 3.1 Interpolation between measured displacement components

A three step interpolation procedure is used:

- i. temporal interpolation of the displacement components measured in all measurement points (here MP1 through MP5, both in MC1452 and in MC1444);
- ii. spatial interpolation along the tunnel axis, of the displacement components which were temporally interpolated according to (i), at measurement points

with the same label, but belonging to two consecutively installed measurement cross-sections (here displacement interpolation between MC1444 and MC1452, at MP1 through MP5); and

- iii. spatial interpolation along the tunnel perimeter, of the MP position-specific displacement component functions gained through temporal and spatial interpolation according to (i) and (ii).

As for the temporal interpolation, displacement components  $q(\varphi_k, z_j; t_i)$  and  $q(\varphi_k, z_j; t_{i+1})$ , measured at time instants  $t_i$  and  $t_{i+1}$  in the  $k$ -th measurement point MP $k$  ( $k = 1, \dots, 5$ ) of the  $j$ -th measurement cross-section MC $j$ , are linearly interpolated according to

$$q(\varphi_k, z_j; t) = q(\varphi_k, z_j; t_i) + \frac{q(\varphi_k, z_j; t_{i+1}) - q(\varphi_k, z_j; t_i)}{t_{i+1} - t_i} (t - t_i); \quad \forall t \in [t_i, t_{i+1}] \quad (1)$$

Longitudinal interpolation between temporal functions  $q(\varphi_k, z_j; t)$  referring to MPs with the same label  $k$ , but belonging to two neighboring MCs (here MC1444 and MC1452), becomes possible once the MP of the younger MC (here MC1452) is installed. Consider interpolation between an MP $k$  ( $k = 1, \dots, 5$ ) located at the *considered* MC (MCc: here MC1452), installed at time instant  $t_{k,0}^c$  at tunnel axis coordinate  $z_c$ , and the corresponding MP $k$  (with the same label  $k$ ) located at the *preceding* MC (MCp: here MC1444), installed at time instant  $t_{k,0}^p$  at tunnel axis coordinate  $z_p$ , (where  $t_{k,0}^p < t_{k,0}^c$  and  $z_p < z_c$ ), see Fig. 4. As an initial condition, all displacements between the two MCs are set equal to zero at time instant  $t = t_{k,0}^c$ , that is  $q(\varphi_k, z; t) = 0$  for  $t = t_{k,0}^c$  and  $z \in [z_p; z_c]$ . In accordance with this initial condition, a linear longitudinal interpolation is carried out between the displacement change at the *preceding* MC,  $q(\varphi_k, z_p; t) - q(\varphi_k, z_p; t_{k,0}^c)$ , and the displacement function at the *considered* MC,  $q(\varphi_k, z_c; t)$ , reading as

$$q(\varphi_k, z; t) = a(t) + b(t)z; \quad z \in [z_p; z_c]; t \geq t_{k,0}^c \quad (2)$$

with

$$a(t) = - \frac{q(\varphi_k, z_c; t)z_p - [q(\varphi_k, z_p; t) - q(\varphi_k, z_p; t_{k,0}^c)]z_c}{z_c - z_p} \quad (3)$$

$$b(t) = \frac{q(\varphi_k, z_c; t) - [q(\varphi_k, z_p; t) - q(\varphi_k, z_p; t_{k,0}^c)]}{z_c - z_p}$$

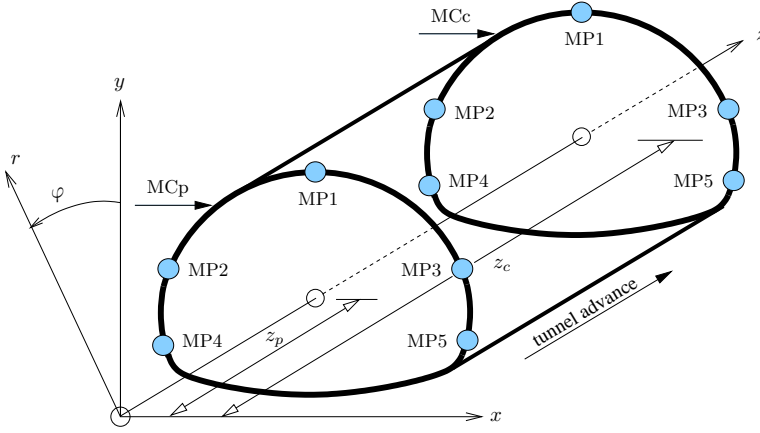


Figure 4: Illustration of the location, along  $z$ -axis, of the *considered* and *preceding* measurement cross-sections (MCc and MCp, respectively)

Spatial interpolation in the circumferential direction is influenced by the construction sequence described in Section 2. As for the top heading, which is considered to be installed first, the time- and longitudinal position-dependent displacement component functions  $q(\varphi_k, z; t)$ ,  $k = 1, 2, 3$  are interpolated quadratically along the positions of MP1, MP2, and MP3, according to

$$q(\varphi, z; t) = c(z; t) + d(z; t) \varphi + e(z; t) \varphi^2; \quad \varphi \in [-\varphi_{tb}; +\varphi_{tb}] \quad (4)$$

with

$$\begin{aligned} c(z; t) &= \frac{q(\varphi_1, z; t)\varphi_2\varphi_3(\varphi_2 - \varphi_3) + q(\varphi_2, z; t)\varphi_3\varphi_1(\varphi_3 - \varphi_1) + q(\varphi_3, z; t)\varphi_1\varphi_2(\varphi_1 - \varphi_2)}{\varphi_1^2(\varphi_3 - \varphi_2) + \varphi_2^2(\varphi_1 - \varphi_3) + \varphi_3^2(\varphi_2 - \varphi_1)} \\ d(z; t) &= \frac{q(\varphi_1, z; t)(\varphi_2^2 - \varphi_3^2) + q(\varphi_2, z; t)(\varphi_3^2 - \varphi_1^2) + q(\varphi_3, z; t)(\varphi_1^2 - \varphi_2^2)}{\varphi_1^2(\varphi_3 - \varphi_2) + \varphi_2^2(\varphi_1 - \varphi_3) + \varphi_3^2(\varphi_2 - \varphi_1)} \\ e(z; t) &= \frac{q(\varphi_1, z; t)(\varphi_3 - \varphi_2) + q(\varphi_2, z; t)(\varphi_1 - \varphi_3) + q(\varphi_3, z; t)(\varphi_2 - \varphi_1)}{\varphi_1^2(\varphi_3 - \varphi_2) + \varphi_2^2(\varphi_1 - \varphi_3) + \varphi_3^2(\varphi_2 - \varphi_1)} \end{aligned} \quad (5)$$

Circumferential displacement interpolation along the left bench is based on the displacements of the top heading-left bench interface (obtained from specification of (4) for  $\varphi = \varphi_{tb}$ ) and of the function  $q(\varphi_4, z; t)$ , see (2), where MP4 is the measurement point installed in the left bench. Interpolation along the left bench becomes possible in a stretch between neighboring MCs, once MP4 is installed in

the younger MC, i.e. in the *considered* MC. As an initial condition at  $t = t_{4,0}^c$ , the displacement field of the left bench is set equal to zero, that is  $q(\varphi, z; t) = 0$  for  $\varphi \in [\varphi_{lb}; \varphi_{bi}]$ ;  $z \in [z_p; z_c]$  and  $t = t_{4,0}^c$ . In accordance with this initial condition, a linear interpolation is carried out between the displacement change at the top heading-left bench interface,  $q(\varphi_{lb}, z, t) - q(\varphi_{lb}, z, t_{4,0}^c)$ , and the displacement function at MP4,  $q(\varphi_4, z; t)$

$$q(\varphi, z; t) = f(z; t) + g(z; t) \varphi; \quad \varphi \in [\varphi_{lb}; \varphi_{bi}]; t \geq t_{4,0}^c \tag{6}$$

with

$$f(z; t) = \frac{[q(\varphi_{lb}, z; t) - q(\varphi_{lb}, z; t_{4,0}^c)] \varphi_4 - q(\varphi_4, z; t) \varphi_{lb}}{\varphi_4 - \varphi_{lb}} \tag{7}$$

$$g(z; t) = \frac{q(\varphi_4, z; t) - [q(\varphi_{lb}, z; t) - q(\varphi_{lb}, z; t_{4,0}^c)]}{\varphi_4 - \varphi_{lb}}$$

An analogous strategy is used for the circumferential interpolation along the right bench. The relevant interpolation function is obtained from (6) and (7) through substitution of  $\varphi_{lb}$ ,  $\varphi_{bi}$ ,  $\varphi_4$  and  $t_{4,0}^c$  by  $-\varphi_{lb}$ ,  $-\varphi_{bi}$ ,  $\varphi_5$  and  $t_{5,0}^c$ , respectively.

The described mode of interpolation provides spatially continuous fields of tunnel shell displacements. At certain interfaces, however, non-smooth displacement functions are obtained, e.g. displacement derivatives at MCs and at the top heading-bench interfaces are discontinuous with respect to  $z$ , and  $\varphi$ , respectively. These two classes of interfaces are characterized by  $C_0$ -continuity, rather than  $C_1$ -continuity of the interpolated displacement fields. This results in strain fields which are discontinuous across these interfaces. This is realistic because these interfaces link neighboring parts of the tunnel shell that are sprayed at different time instants, exhibit different ages resulting in different degrees of hydration and, hence, different material properties.

### 3.2 Interpolation strategies I and II

Along the lines of earlier approaches [Hellmich, Mang, and Ulm (2001); Hellmich (1999); Lackner, Macht, and Mang (2006); Macht, Lackner, Hellmich, and Mang (2003)], our first choice for three scalar quantities  $q(\varphi_k, z_j; t_i)$  defining displacement vectors, are their components with respect to the fixed Cartesian coordinate frame of Fig. 1, i.e.  $u_x$ ,  $u_y$  and  $u_z$  measured in MPk of MCj at  $t_i$ . This choice, referred to as “interpolation strategy I”, seems natural given the fact that these components are actually recorded by the laser-optical system. Still, for certain deformation states, it may be suboptimal. Let us consider the state of uniform radial squeezing [Fig. 5(a)], which is preferentially defined in terms of cylindrical displacement

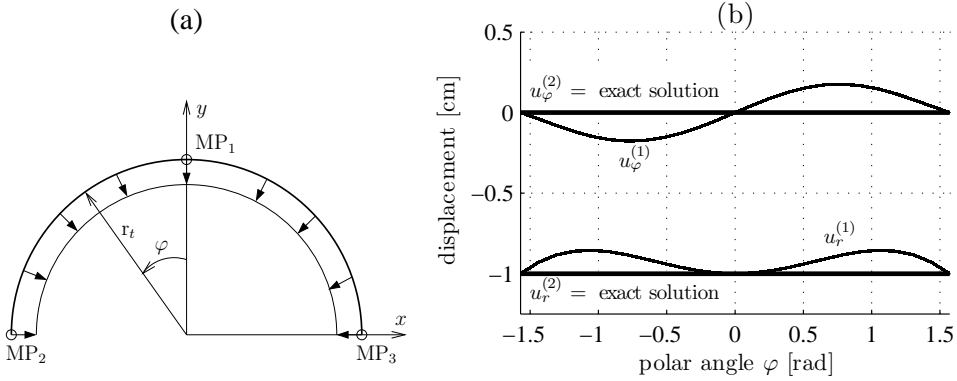


Figure 5: Reconstruction of displacement fields for uniform radial squeezing  $u_r = -1 \text{ cm} = \text{const}$ ,  $u_\varphi = u_z = 0$ , considering a top heading with  $r_t = 6.20 \text{ m}$  and  $\pm\varphi_{tb} = \pm\frac{\pi}{2}$ , starting from displacement “measurements”  $(u_x)_{MP1} = (u_z)_{MP1} = 0 \text{ cm}$ ,  $(u_y)_{MP1} = -1 \text{ cm}$ ;  $(u_y)_{MP2} = (u_z)_{MP2} = 0 \text{ cm}$ ,  $(u_x)_{MP2} = +1 \text{ cm}$ ;  $(u_y)_{MP3} = (u_z)_{MP3} = 0 \text{ cm}$ ,  $(u_x)_{MP3} = -1 \text{ cm}$ ; results from interpolation strategy I:  $u_r^{(1)}$  and  $u_\varphi^{(1)}$  [interpolation according to (1), (2), (4) and (6) is followed by transformation according to (8)] and from interpolation strategy II:  $u_r^{(2)}$  and  $u_\varphi^{(2)}$  [transformation according to (8) is followed by interpolation according to (1), (2), (4) and (6)]

components  $u_r$ ,  $u_\varphi$ ,  $u_z$ , which are related to the Cartesian components  $u_x$ ,  $u_y$ , and  $u_z$  through

$$\begin{bmatrix} u_r \\ u_\varphi \\ u_z \end{bmatrix} = \begin{bmatrix} \cos(\varphi + \frac{\pi}{2}) & \sin(\varphi + \frac{\pi}{2}) & 0 \\ -\sin(\varphi + \frac{\pi}{2}) & \cos(\varphi + \frac{\pi}{2}) & 0 \\ 0 & 0 & 1 \end{bmatrix} \cdot \begin{bmatrix} u_x \\ u_y \\ u_z \end{bmatrix} \quad (8)$$

Radial squeezing is characterized by homogeneous radial displacement components  $u_r$  as well as zero circumferential and axial components:  $u_\varphi = u_z = 0$ . However, the choice of  $q(\varphi_k, z_j; t_i)$  as  $u_x$ ,  $u_y$ , and  $u_z$ , respectively, yields displacement field approximations deviating from the actual squeezing characteristics [see Fig. 5(b)]. This motivates introduction of an alternative interpolation strategy (called interpolation strategy II) where the displacement components are first transformed by means of (8) into the shell-intrinsic moving  $r$ - $\varphi$ - $z$  base frame. Thereafter, the components  $u_r$ ,  $u_\varphi$  and  $u_z$  (in  $MPk$  of  $MCj$  at  $t_i$ ) are interpolated according to (1), (2), (4), and (6), in order to construct the displacement fields  $u_r(\varphi, z; t)$ ,  $u_\varphi(\varphi, z; t)$  and  $u_z(\varphi, z; t)$ . Remarkably, interpolation strategy II is able to reconstruct the exact displacement field for uniform radial squeezing (see Fig. 5).

#### 4 Reconstructing the strain fields of the tunnel shell from the interpolated displacement field using kinematics from linear thin shell theory

Next, we use the interpolation-derived displacement fields  $\underline{u}(\varphi, z; t)$  for reconstructing the strain fields  $\underline{\underline{\varepsilon}}(\rho, \varphi, z; t)$  throughout the tunnel shell (see Fig. 6 for radial coordinate  $\rho$  measured from a reference surface). Therefore, we consider that NATM tunnel shells are, generally speaking, thin shells, i.e. their thickness  $h$  is very small as compared to the smallest curvature radius  $R$  of the shell's reference surface [Basar and Krätzig (2001); Koiter and Simmonds (1972)]:

$$\frac{h}{\min R} \ll 1 \tag{9}$$

The aforementioned reference surface may coincide, but need not necessarily be identical with the midsurface of the shell.

For describing the deformation states of such thin shells, we first consider the position vector  $\underline{X}$  labeling points on the reference surface of the *undeformed* cylindrical shell (Fig. 6). The position vector  $\underline{X}$  is expressed in the orthonormal basis  $\underline{e}_x, \underline{e}_y$

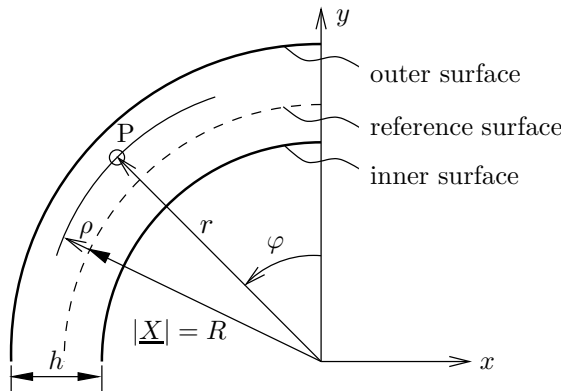


Figure 6: Definitions of reference surface and moving radial coordinate  $\rho$  of tunnel shell

and  $\underline{e}_z$  of the fixed Cartesian coordinate frame, the origin of which is located on the cylinder axis. Thus, we have

$$\underline{X}(\varphi, z) = R \cos(\varphi + \frac{\pi}{2}) \underline{e}_x + R \sin(\varphi + \frac{\pi}{2}) \underline{e}_y + z \underline{e}_z \tag{10}$$

In the *undeformed* configuration, (i) the covariant in-plane base vectors  $\underline{A}_\varphi$  and  $\underline{A}_z$  of the reference surface are tangential to the parameter lines of  $\varphi$  and  $z$ , and (ii) the out-of-plane unit base vector  $\underline{A}_r$ , of the reference surface, also referred to as the shell director, is standardly defined as a unit vector [Cirak, Ortiz, and Schröder (2000)]; reading as

$$\underline{A}_\alpha(\varphi, z) = \frac{\partial \underline{X}(\varphi, z)}{\partial \alpha}; \quad \alpha = \varphi, z \quad \text{and} \quad \underline{A}_r = \frac{\underline{A}_\varphi \wedge \underline{A}_z}{|\underline{A}_\varphi \wedge \underline{A}_z|} \quad (11)$$

The covariant base vectors at points with radial distance  $\rho$  (Fig. 6) from the reference surface read as [Cirak, Ortiz, and Schröder (2000)]

$$\underline{G}_\alpha(\rho, \varphi, z) = \underline{A}_\alpha(\varphi, z) + \rho \frac{\partial \underline{A}_r(\varphi, z)}{\partial \alpha}; \quad \alpha = \varphi, z; \quad \text{and} \quad \underline{G}_r = \underline{A}_r \quad (12)$$

The inner products of these base vectors give access to the covariant components of the metric tensor

$$G_{ij} = \underline{G}_i \cdot \underline{G}_j; \quad i, j = r, \varphi, z \quad (13)$$

These components are directly linked to the strains in the shell, once the *deformed* configuration of the reference surface is also considered.

In the *deformed* configuration, the points belonging to the reference surface are labelled by  $\underline{x}$ , which are expressed as the sum of their initial counterparts  $\underline{X}$  and the displacement vectors  $\underline{u}$

$$\underline{x}(\varphi, z) = \underline{X}(\varphi, z) + \underline{u}(\varphi, z) \quad (14)$$

Related covariant base vectors  $\underline{a}_\varphi$ ,  $\underline{a}_z$ , and  $\underline{a}_r$  follow, by analogy to (11), as

$$\underline{a}_\alpha = \frac{\partial \underline{x}}{\partial \alpha} = \frac{\partial \underline{X}}{\partial \alpha} + \frac{\partial \underline{u}}{\partial \alpha} = \underline{A}_\alpha + \frac{\partial \underline{u}}{\partial \alpha}; \quad \alpha = \varphi, z \quad \text{and} \quad \underline{a}_r = \frac{\underline{a}_\varphi \wedge \underline{a}_z}{|\underline{a}_\varphi \wedge \underline{a}_z|} \quad (15)$$

In accordance with slenderness condition (9), we adopt the so-called Kirchhoff-Love assumption [Love (1944)], stating essentially that points lying on a normal to the *undeformed* reference surface stay, during deformation, on a straight line normal to the *deformed* reference surface (generalized Euler-Bernoulli hypothesis).

Accordingly, the base vectors  $\underline{g}_\alpha$  ( $\alpha = \varphi, z$ ) and  $\underline{g}_r$  at distance  $\rho$  from the reference surface read as

$$\underline{g}_\alpha = \underline{a}_\alpha + \rho \frac{\partial \underline{a}_r}{\partial \alpha}; \quad \alpha = \varphi, z; \quad \text{and} \quad \underline{g}_r = \underline{a}_r \quad (16)$$

They give access to the covariant components of the metric tensor of the deformed shell, by analogy to (13), as

$$g_{ij} = \underline{g}_i \cdot \underline{g}_j; \quad i, j = r, \varphi, z \quad (17)$$

Finally, metric tensors (13) and (17) give access to the linearized strain tensor as [Cirak, Ortiz, and Schröder (2000)]

$$e_{ij} = \frac{1}{2}(g_{ij} - G_{ij}); \quad \Rightarrow \quad \varepsilon_{ij} = \frac{e_{ij}}{\sqrt{g_{ii}g_{jj}}} \quad (\text{no sum over } i, j = r, \varphi, z) \quad (18)$$

The strain tensor  $e_{ij}$  in (18)<sub>1</sub> refers to the non-normalized system of base vectors  $\underline{g}_\varphi$ ,  $\underline{g}_z$ , and  $\underline{g}_r$ , while normalization according to (18)<sub>2</sub> delivers *physical* strains  $\varepsilon_{ij}$  [Fung (1965)].

The kinematic assumptions of linear thin shell theory (16) imply that  $\varepsilon_{rr} = \varepsilon_{\varphi r} = \varepsilon_{r\varphi} = \varepsilon_{rz} = \varepsilon_{rz} = 0$ . Hence only  $\varepsilon_{\varphi\varphi}$ ,  $\varepsilon_{zz}$  and  $\varepsilon_{\varphi z} = \varepsilon_{z\varphi}$  are non-zero components in the present approach.

## 5 Determining tunnel shell stresses from strains based on micromechanical models for hydrating shotcrete

In order to relate the evolution of strain fields reconstructed through displacement interpolation (Section 3) and thin shell theory (Section 4) to corresponding stresses and forces in the tunnel shell, we recall that, besides stresses, temperature changes are governing the strains in early-age sprayed concrete. The temperature changes mainly result from the exothermic nature of the hydration reaction between cement and water. Hence, the overall liberated heat during hydration depends on the shotcrete mixture characteristics, i.e. the water-cement ratio  $w/c$  and the aggregate-cement ratio  $a/c$ . We here consider a typical shotcrete mixture with  $w/c = 0.5$  and  $a/c = 5$ . Given a typical heat value of  $H_{\text{cement}} = 500$  kJ/kg cement liberated upon complete hydration [Byfors (1980)], the aforementioned mixture characteristics imply a shotcrete-specific latent heat of hydration,  $H_{sc}$ , of magnitude

$$H_{sc} = \frac{1}{(w/c + a/c + 1)} H_{cement} \rho_{concrete} = 191150 \text{ kJ/m}^3 \text{ shotcrete} \quad (19)$$

when considering  $\rho_{concrete} = 2485 \text{ kg/m}^3$  as a typical value for the mass density of sprayed concrete. In order to quantify the spatio-temporal effects of this heat release all over the tunnel shell, a thermochemical analysis [Hellmich (1999)] of the shotcrete shell and the surrounding soil is performed. It comprises simultaneous solution of the energy conservation law [first law of thermodynamics, based on specific heat capacities of shotcrete and soil amounting to  $2428 \text{ kJ/(m}^3\text{K)}$  [Hellmich (1999)] and  $2300 \text{ kJ/(m}^3\text{K)}$  [Smith and Booker (1996)], and on the hydration heat of (19)], of Fourier's heat conduction law (with the thermal conductivity coefficient of shotcrete as  $12.6 \text{ kJ/(mhK)}$  [Hellmich (1999)], and that of soil as  $7.2 \text{ kJ/(mhK)}$  [Smith and Booker (1996)]), and of the hydration kinetics laws quantified through the chemical affinity concept [Ulm and Coussy (1996)] with the material parameters given in [Hellmich, Ulm, and Mang (1999)]. As a result of corresponding non-linear Finite Element analyses (with initial shotcrete temperature  $T_{ini}$  of  $12^\circ\text{C}$ , initial soil temperature of  $10^\circ\text{C}$ , and air temperature of  $0^\circ\text{C}$ , as well as convective heat transfer coefficient of  $14.4 \text{ kJ/(m}^2\text{hK)}$  [Acker, Fourier, and Malier (1986)]), we obtain temporal evolutions of temperature and hydration degree fields across the tunnel shell thickness of 30 cm, see Figs. 7 and 8.

In order to relate the fields of temperature to corresponding thermal strains  $\underline{\underline{\epsilon}}_T$ , we consider an isotropic thermal dilatation of  $\alpha_T = 10^{-5}/^\circ\text{C}$ , so that

$$\underline{\underline{\epsilon}}_T(\rho, t) = [T(\rho, t) - T_{ini}] \alpha_T \underline{\underline{1}} \quad (20)$$

The remaining strains, i.e. the difference between the total strains reconstructed from displacement-interpolation and thin shell theory, and the thermal strains,

$$\underline{\underline{\epsilon}}_M(\rho, t) = \underline{\underline{\epsilon}}(\rho, t) - \underline{\underline{\epsilon}}_T(\rho, t) \quad (21)$$

are termed "mechanical" strains. They provoke mechanical stresses. For estimation of the latter, we need to consider the dependence of shotcrete's mechanical properties on the hydration degree, as to account for the fields of varying mechanical properties resulting from the hydration degree fields of Fig. 8.

In order to quantify these mechanical stresses, the creep (viscoelastic) behavior of shotcrete needs to be considered. Viscoelasticity means that there is no unique

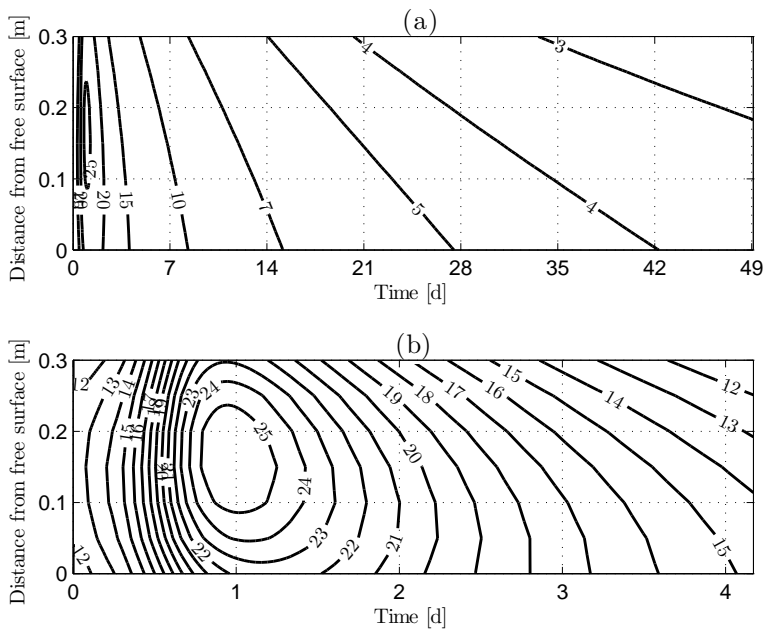


Figure 7: Evolution of temperature, across the tunnel shell thickness, due to heat of hydration: (a) from placement of shotcrete through 50 days (b) zoom out for the first 4 days after placement of shotcrete

stress-strain relationship, but that time-invariant (constant) mechanical strains provoke mechanical stresses which decrease over time (this is standardly referred to as relaxation). In the same sense, prescribed (time-invariant) stress loading on the material provokes strains which increase over time (this is standardly referred to as creep). What makes the situation more intricate in shotcrete (and in concrete in general) is that the relaxation and creep functions describing stress decrease and strain increase, respectively, are not constant, but they depend on the maturity of the (aging) material, i.e. on its degree of hydration. Hence, the standard creep and relaxation functions (e.g. those used in the polymer science [Knauss (2003)]) can be applied to concrete only during an infinitely short period (during which the material exhibits a constant microstructure, i.e. it is not aging). In other words, a consistent extension of non-aging creep functions to aging materials consists of deriving such functions with respect to time,

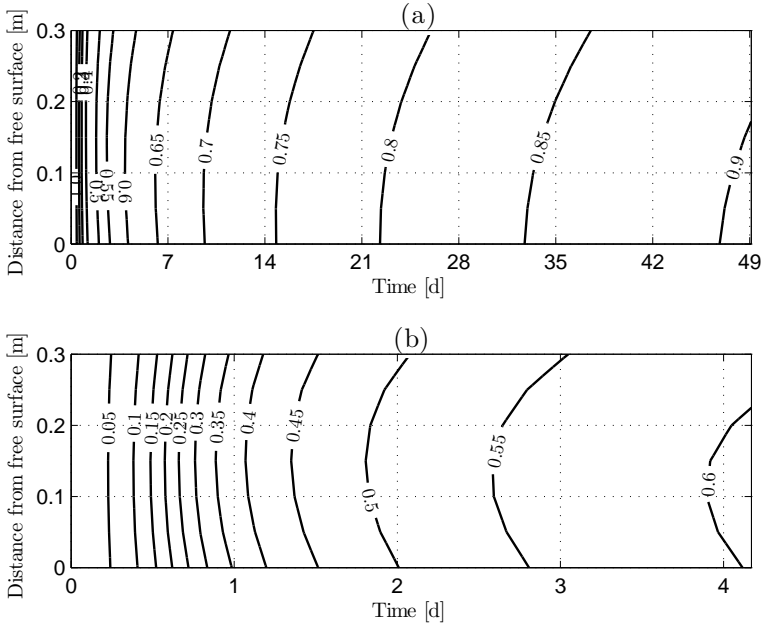


Figure 8: Evolution of hydration degree across the tunnel shell thickness: (a) from placement of shotcrete through 50 days, (b) zoom out for the first 4 days after placement of shotcrete

$$\frac{\partial \underline{\underline{\underline{\varepsilon}}}_M(t)}{\partial t} = \underline{\underline{\underline{\mathcal{J}}}}[\underline{\underline{\underline{\xi}}}(t), 0] : \frac{\partial \underline{\underline{\underline{\sigma}}}(t)}{\partial t} + \int_{-\infty}^t \frac{\partial \underline{\underline{\underline{\mathcal{J}}}}[\underline{\underline{\underline{\xi}}}(t), t - \tau]}{\partial t} : \frac{d\underline{\underline{\underline{\sigma}}}(\tau)}{d\tau} d\tau \quad (22)$$

and of subsequently accumulating such incremental creep responses  $\dot{\underline{\underline{\underline{\varepsilon}}}}_M(t)$ , as was recently proposed by [Scheiner and Hellmich (2009)]. In (22),  $\frac{\partial \underline{\underline{\underline{\mathcal{J}}}}[\underline{\underline{\underline{\xi}}}(t), t - \tau]}{\partial t}$  is the rate of the (isotropic) creep tensor related to a material of hydration degree  $\underline{\underline{\underline{\xi}}}$ , loaded at time  $\tau$ , reading as

$$\frac{\partial \underline{\underline{\underline{\mathcal{J}}}}[\underline{\underline{\underline{\xi}}}(t), t - \tau]}{\partial t} = 3 \frac{\partial k_c}{\partial t}[\underline{\underline{\underline{\xi}}}(t), t - \tau] \underline{\underline{\underline{\mathbb{J}}}} + 2 \frac{\partial \mu_c}{\partial t}[\underline{\underline{\underline{\xi}}}(t), t - \tau] \underline{\underline{\underline{\mathbb{K}}}} \quad (23)$$

with

$$\begin{aligned}
 k_c[\xi(t), t - \tau] &= \frac{1}{3} \mathcal{J}_{1111}[\xi(t), t - \tau] + \frac{2}{3} \mathcal{J}_{1122}[\xi(t), t - \tau] \\
 \mu_c[\xi(t), t - \tau] &= \frac{1}{2} \mathcal{J}_{1111}[\xi(t), t - \tau] - \frac{1}{2} \mathcal{J}_{1122}[\xi(t), t - \tau]
 \end{aligned}
 \tag{24}$$

and also in (22),  $\underline{\underline{\mathcal{J}}}[\xi(t), 0]$  is the instantaneous response of a material of hydration degree  $\xi$ , being identical to the elastic compliance tensor, which is the inverse of the elastic stiffness tensor  $\underline{\underline{\mathbb{C}}}_{sc}$ ,

$$\underline{\underline{\mathbb{C}}}_{sc}[\xi(t)] = 3k_{sc}[\xi(t)]\underline{\underline{\mathbb{J}}} + 2\mu_{sc}[\xi(t)]\underline{\underline{\mathbb{K}}}
 \tag{25}$$

with the bulk modulus  $k_{sc}$  and the shear modulus  $\mu_{sc}$ . In (25), the fourth-order tensors  $\underline{\underline{\mathbb{J}}}$  and  $\underline{\underline{\mathbb{K}}}$  are defined as  $\underline{\underline{\mathbb{J}}} = (1/3)\underline{\underline{\mathbb{1}}} \otimes \underline{\underline{\mathbb{1}}}$  and  $\underline{\underline{\mathbb{K}}} = \underline{\underline{\mathbb{I}}} - \underline{\underline{\mathbb{J}}}$ , where  $\underline{\underline{\mathbb{1}}}$  is the second-order unity tensor with components  $\delta_{ij}$  (Kronecker delta) and  $\underline{\underline{\mathbb{I}}}$  is the symmetric fourth-order unity tensor with components  $I_{ijkl} = 1/2(\delta_{ik}\delta_{jl} + \delta_{il}\delta_{jk})$ .

The creep functions  $\underline{\underline{\mathcal{J}}}[\xi(t), t - \tau]$  also depend on the shotcrete mixture characteristics, i.e. the water-cement ratio  $w/c$  and the aggregate-cement ratio  $a/c$ . These relationships can be established on the basis of the Powers-Acker hydration model [Powers and Brownyard (1948); Acker, Fourier, and Malier (1986)], establishing the interdependence between  $\xi$ ,  $w/c$ , and  $a/c$ , on the one hand, and the volume fractions of clinker (anhydrous cement), of water, of hydrates, and of aggregates within a piece of shotcrete, on the other hand. These volume fractions can finally be translated, by means of a micro-viscoelasticity model for concrete [Scheiner and Hellmich (2009)] based on mixture-independent ‘universal’ (visco-elastic) properties of cement, hydrates, water, and aggregates, into mixture-specific mechanical properties of shotcrete. Corresponding results for the shotcrete mixture considered herein, with  $w/c = 0.5$ ,  $a/c = 5$ , and with material component properties as given in Table 2, are illustrated in Fig. 9 (where  $k_{sc}(\xi)$  and  $\mu_{sc}(\xi)$  are the elastic properties introduced in (25), being related to  $\underline{\underline{\mathcal{J}}}[\xi(t), 0]$ ) and Fig. 10 [where the components  $\partial \mathcal{J}_{1111} / \partial t$  and  $\partial \mathcal{J}_{1122} / \partial t$  are related to (22)-(24)]. Along similar lines, the microelasto-brittle model of [Pichler, Scheiner, and Hellmich (2008)] provides us with the  $w/c$ -,  $a/c$ -, and  $\xi$ -specific uniaxial compressive strength  $f_c$  of shotcrete (see Fig. 9 for  $w/c = 0.5$ ,  $a/c = 5$ , and with material component properties as given in Table 2). Both aforementioned micromechanics models are set in the framework of random homogenization theory [Zaoui (2002)], which, given its extreme

Table 2: Elastic properties of elementary components of shotcrete (for viscoelastic and strength properties of hydrates, see [Scheiner and Hellmich (2009)] and [Pichler, Scheiner, and Hellmich (2008)]) ; A2001 ... [Acker (2001)], U2004 ... [Ulm, Constantinides, and Heukamp (2004)], L1993 ... [Laplante (1993)], B1993 ... [Bilaniuk and Wong (1993)]

Elementary components	Bulk modulus (GPa)	Shear modulus (GPa)	Source
Clinker	116.7	53.8	A2001
Hydrates	14.1	8.9	U2004
Aggregates	54.2	25.0	L1993
Water	2.3	0.0	B1993
Air	0.0	0.0	

computational efficiency, has turned out to be a surprisingly precise prognosis tool when compared to much more expending representations of material microstructure, such as full 3D Finite Element or Boundary Element representations [Böhm, Han, and Eckschlager (2004)], [Okada, Fukui, and Kumazawa (2004)], [Pyo and Lee (2009)], [Sanahuja, Dormieux, Meille, Hellmich, and Fritsch (2010)].

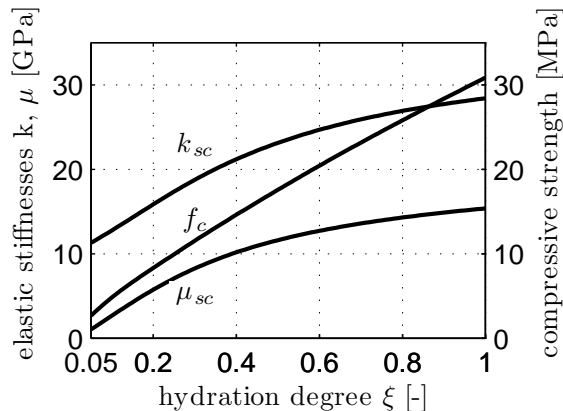


Figure 9: Evolution of elastic shear modulus  $\mu_{sc}$ , elastic bulk modulus  $k_{sc}$ , and uniaxial compressive strength  $f_c$  of shotcrete over hydration degree for  $w/c = 0.50$  and  $a/c = 5$ , values predicted by the micromechanical models of [Scheiner and Hellmich (2009)], [Pichler, Hellmich, and Eberhardsteiner (2009)] and [Pichler, Scheiner, and Hellmich (2008)]

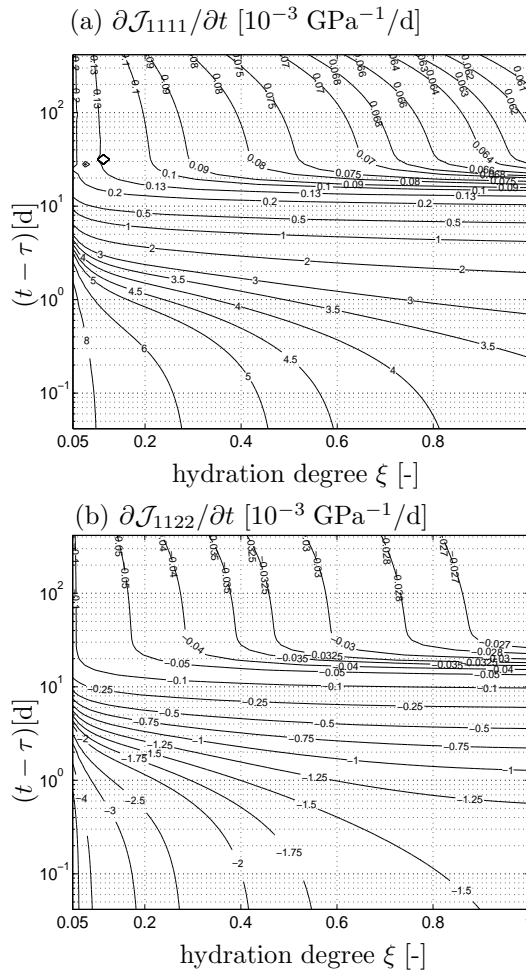


Figure 10: Creep rates of shotcrete with  $w/c = 0.50$  and  $a/c = 5$ : (a)  $\partial \mathcal{J}_{1111} / \partial t$  and (b)  $\partial \mathcal{J}_{1122} / \partial t$ , values predicted by the model of [Scheiner and Hellmich (2009)]

Creep functions  $\mathcal{J}$  as introduced in (22), relating increases in stress rates *linearly* to strain rates, are admissible for moderate loading conditions. However, if the applied stress reaches more than 40% of the concrete’s strength, the material undergoes some damage, which results in a softer response, i.e. the creep function  $\mathcal{J}$  is increasing. Since a direct micromechanical representation of this quite complex, not fully understood damaging phenomenon is out of reach for the moment, we here adopt the affinity concept for nonlinear creep, put forward by [Ruiz, Muttoni,

and Gambarova (2007)]. These authors state that, under constant uniaxial compressive strength, the creep response is affine to the creep response below that critical stress level, and that the creep magnification factor  $\eta$  quantifying this affinity of functions reads as

$$\eta = 1 + 2 \left( \frac{|\sigma_c|}{f_c} \right)^4 \quad \text{for } \frac{|\sigma_c|}{f_c} > 0.4; \quad \eta = 1 \quad \text{otherwise} \quad (26)$$

with  $|\sigma_c|$  being the absolute value of uniaxial compressive stress applied to the investigated concrete sample. Given two-dimensional, rather than one-dimensional stress states prevailing in shotcrete tunnel shells, we are left with extending the 1D-specific “level of loading”  $|\sigma_c|/f_c$  to a 2D case; and therefore, we adopt a Drucker-Prager criterion

$$\mathcal{L}(\underline{\underline{\sigma}}) = \frac{\alpha_{DP} \text{tr} \underline{\underline{\sigma}} + \sqrt{\underline{\underline{s}} : \underline{\underline{s}}}}{k_{DP}} \leq 1 \quad (27)$$

In (27),  $\underline{\underline{s}} = \underline{\underline{\sigma}} - (\text{tr} \underline{\underline{\sigma}}/3)\underline{\underline{1}}$  denotes the stress deviator. The dimensionless parameter  $\alpha_{DP}$  and the strength-like quantity  $k_{DP}$  are related to the uniaxial and biaxial compressive strengths  $f_c$  and  $f_b$  of shotcrete

$$\alpha_{DP} = \sqrt{\frac{2}{3}} \frac{\kappa - 1}{2\kappa - 1}; \quad k_{DP} = \sqrt{\frac{2}{3}} \left( 1 - \frac{\kappa - 1}{2\kappa - 1} \right) f_c; \quad \kappa = \frac{f_b}{f_c} \quad (28)$$

where  $\kappa = 1.2$  follows from standard tests [CEB-FIP (1990)].

Specifying (27) for uniaxial compression  $\underline{\underline{\sigma}} = -|\sigma_c| \underline{\underline{e}}_1 \otimes \underline{\underline{e}}_1$  results in  $\mathcal{L}(\underline{\underline{\sigma}}) = |\sigma_c|/f_c$ , so that extension of (26) to the 2D case reads as

$$\eta = 1 + 2(\mathcal{L})^4 \quad \text{for } \mathcal{L} > 0.4; \quad \eta = 1 \quad \text{otherwise} \quad (29)$$

with  $\mathcal{L}$  according to (27). On the basis of (29), we extend (22) to the nonlinear creep regime beyond 40% level of loading, through introducing a nonlinear creep function as

$$\frac{\partial \underline{\underline{\mathcal{J}}}_{nl}[\underline{\underline{\xi}}(t), t - \tau]}{\partial t} = \underbrace{\left[ 1 + 2 \left( \frac{\alpha_{DP} \text{tr} \underline{\underline{\sigma}} + \sqrt{\underline{\underline{s}} : \underline{\underline{s}}}}{k_{DP}} \right)^4 \right]}_{\eta} \frac{\partial \underline{\underline{\mathcal{J}}}[\underline{\underline{\xi}}(t), t - \tau]}{\partial t} \quad (30)$$



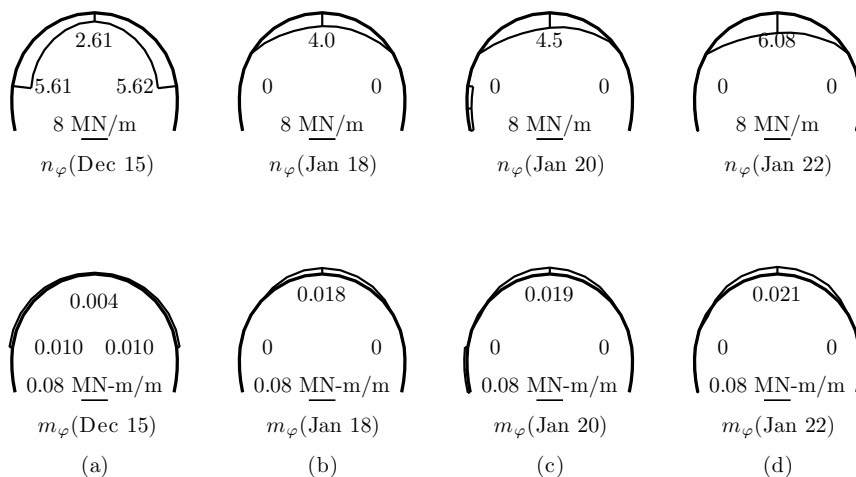


Figure 11: Distribution of circumferential normal forces  $n_\varphi$  and bending moment  $m_\varphi$ , at critical dates, for interpolation strategy I (a) Dec 15 (b) Jan 18 (c) Jan 20 and (d) Jan 22

tunnel shell as the reference surface), the analysis proposes, for Dec 15, altogether compressive normal forces, which are almost symmetric with respect to the crown, and they exhibit concentrations at the lateral parts of the top heading (Fig. 11). On Jan 18, one day prior to the installation of the left bench, the analysis proposes that the compressive circumferential forces are still symmetric, but concentrate in the crown and the very lateral parts of the top heading exhibit small tensile forces. Excavation of the left bench on Jan 19 results in an increase of the compressive force level in the crown region, and in a shift of this region towards the newly installed shell part. Excavation of the right bench on Jan 21 again increases the compressive force level in the crown region and reduces the amount of asymmetry of this region.

Stress profiles over the shell thickness do not show pronounced fluctuations, resulting in very small bending moments (Fig. 11). Still, we note that initially the maximum bending moment is obtained at the lateral ends of the top heading, while in Jan 1998, around installation of the benches, maximum bending moments are proposed to be situated in the crown.

When employing interpolation strategy II (interpolation of polar displacement components as described in Section 3.2 – and choice of the inner surface of the tunnel shell as the reference surface), the analysis proposes, for Dec 15, altogether compressive normal forces, which reach a maximum in the crown, and are almost twice

as small at the left end as compared with the right end (Fig. 12). On Jan 18, one day

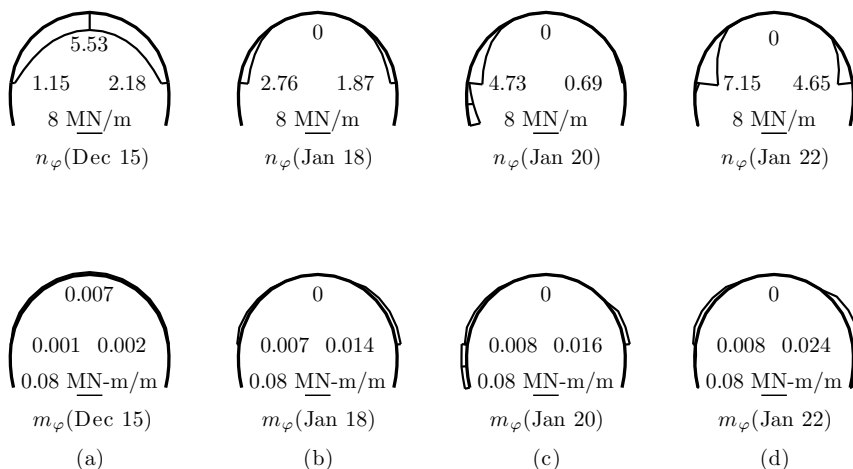


Figure 12: Distribution of circumferential normal forces  $n_\varphi$  and bending moment  $m_\varphi$ , at critical dates, for interpolation strategy II (a) Dec 15 (b) Jan 18 (c) Jan 20 and (d) Jan 22

prior to the installation of the left bench, the analysis proposes that the crown region exhibits small tensile forces while compressive circumferential forces prevail in the lateral parts of the top heading, with a higher force level at the left side. Bench excavation has practically no influence on the unloaded crown region. Excavation works and the related installation of the left bench, however, significantly increase the compressive forces in the directly connected part of the top heading, whereas the right bench region shows pronounced unloading (on Jan 20). Excavation of the right bench, in turn, results in a significant reloading of both lateral parts of the top heading, whereby the load increase is more pronounced at the right side (Jan 22). Bending moments are again very small. Still, we note that initially, the maximum bending moment is situated in the crown, while in Jan 1998, around installation of the benches, maximum bending moments are situated close to the benches.

The latter results change by less than 5% if the midsurface, instead of the inner surface of the tunnel shell, is chosen as reference surface. We also checked the sensitivity of force estimation to perturbations of the lining reference configuration, by increasing the radius of curvature of the top heading by 5% (i.e. by roughly 30 cm). This caused decrease of the circumferential forces, by a maximum of about 5%, occurring once the shell has considerably stiffened (at around 4 weeks after installation and later). At early age, the sensitivity of force estimation to

perturbations of the lining reference configuration is negligible. Hence, selection of the reference surface or a change in its curvature is of minor importance when estimating the stress state in the tunnel. In contrast, choice of interpolation strategy I or II, resulted in qualitatively different estimates for the load carrying behavior of the tunnel shell. They deserve further discussion:

Interpolation strategy I suggests large circumferential forces being introduced from the two ends into the top heading on Dec 15 (see Fig. 11), and bending moments which are larger at the top heading's ends than at the crown. This, in turn, would suggest rather clamped supports at the ends of the top heading on Dec 15. However, no structural means are foreseen in shotcrete tunnelling as to provide the realization of such clamped supports. This renders the load carrying behavior of the tunnel shell when estimated through interpolation strategy I as rather unrealistic.

In contrast, interpolation strategy II suggests circumferential forces which are significantly larger in the crown than in the lateral parts and at the ends of the top heading on Dec 15 (see Fig. 12), and the same holds for the bending moments. This, in turn, suggests rather free ends of the top heading on Dec 15, which seems realistic for shotcrete tunnel shells, since no precautions are made as to maximize the load transfer from tunnel shell to the surrounding rock at the top heading's ends.

The overall compressive loading of the tunnel shell is consistent with a qualitative interpretation of the displacement data of Figure 2: Excavation of the top heading at MC1452 (at Dec 14), together with the following forward-driving of the tunnel face, reduces the support of soil mass lying above the newly installed tunnel cross section, leading therefore to a significant downward movement of the tunnel crown, MP1. At the same time, large plastic zones exhibiting significant vertical compaction emerge adjacent to the lateral measurement points MP2 and MP3. Since these zones are probable to extend well above and particularly below these measurement points [Huang, Xu, and Zhou (2009)], they result in downward movements of MP2 and MP3. The latter are, however, smaller than that of MP1, so that the tunnel shell is compressed. This compression is further magnified through the inward movement of MP2 and MP3, resulting also from the aforementioned plastic soil deformation adjacent to these measurement points.

The situation is quite different when it comes to bench excavation (Jan 19): Then, the matter above the newly excavated areas is well supported through the stiffened top heading shell, which then extends well beyond MC1452, along the longitudinal (track) direction of the tunnel. Hence, no downward movement of measurement points is observed. However, redistribution of vertical forces below MP2 and MP3, away from the newly excavated area, results in new stress concentrations and additional plasticizing of the soil adjacent to the newly excavated benches. On the one hand, this stress concentration leads again to strong inward movements of MP2 and

MP3. On the other hand, plastic soil compaction in this region causes de-loading of the tunnel crown. This is reflected by crown heaving (upward movement of MP1), and by quite significant reduction of compressive circumferential strains there, which, given the highly stiffened nature of the shell, even provoke some tensile stresses there.

At the same time, the forces in the rock mass have to circumvent the formerly not excavated benches, which leads to high force concentrations in the already mature and stiff lower parts of the top heading. After excavation of the left bench and installation of new shotcrete walls there, an increase of the circumferential forces in that part of the shell is observed on Jan 20 (see Fig. 12), as it is on right-hand side, once the bench has been excavated there on Jan 22 (see Fig. 12). This is seen as realistic loading scenario, consistent with the structural provisions made when driving the Sieberg tunnel. Therefore, we regard interpolation strategy II as superior to strategy I, in terms of realistically representing the load carrying behavior of shotcrete tunnel shells.

It is interesting to compare the maximum circumferential forces in the Sieberg tunnel cross-section with 20 m overburden, to those measured in and simulated for a similarly sized concrete tunnel shell, but with 300 m overburden of highly fractured carboniferous rock formation [Pellet (2009)], [Rettighieri, Triclot, Mathieu, Berla, and Panet (2008)]. The latter forces amount to 18 MN/m (simulated) and 14 MN/m (measured), versus 7 MN/m encountered in the Sieberg tunnel (see Fig. 12). On the other hand, in a tunnel with smaller diameter and lower overburden than the Sieberg tunnel, lower circumferential forces of about 2 MN/m were measured [Möller and Vermeer (2008)]. It makes also sense that simplified numerical simulations which do not account for plastic deformations in the ground suggest too small circumferential forces, e.g. [Städling and Winselmann (1998)] report circumferential forces on the order of 2 MN/m in a tunnel shell which compares to the Sieberg tunnel, in terms of both cross-section and overburden. On the other hand, for another Sieberg-like tunnel, elastoplastic simulations [Weissbach and Juli (1984)] suggest axial forces comparable to those of Fig. 12. In such simulations, proper consideration of plastic soil compaction, e.g. through cap models [Sandler and Rubin (1979)], [Hofstetter, Simo, and Taylor (1993)], is of central importance, since classical Mohr-Coulomb or Drucker-Prager models may underestimate the size of the plasticized zones in the ground, leading to comparatively lower circumferential forces in the tunnel shell [Oetl, Stark, and Hofstetter (1998)], [Hellmich and Mang (1999)].

### 7 Safety assessment of tunnel shell

Finally, it is interesting to relate the stresses estimated in the tunnel shell, to the ultimate stresses (strength) the sprayed concrete can sustain. As regards compressive stress states, they will be quantified through the level of loading (also called utilization degree) given in (27). In case of shotcrete microcracking under (small) tensile loads, the maximum tensile strain  $\max(\epsilon_{\varphi\varphi}, \epsilon_{zz})$  is compared with a critical tensile strain of the steel fabric reinforcement (SFR),  $\epsilon_h$ . The latter is chosen to be the steel strain at the end of the yield plateau, i.e. the strain at the beginning of the hardening phase in a uniaxial tension test. Hence, the SFR related level of loading (in case of tensile stresses) reads as

$$\mathcal{L}(\underline{\epsilon}) = \frac{\max(\epsilon_{\varphi\varphi}, \epsilon_{zz})}{\epsilon_h} \tag{35}$$

with  $\epsilon_h = 2.2\%$ .

In order to come up with a structural degree of utilization at a considered time instant, the level of loading field  $\mathcal{L}(\rho, \varphi, z_c; t)$  is first averaged over the shell thickness

$$\overline{\mathcal{L}}(\varphi, z_c; t) = \frac{1}{h} \int_h \mathcal{L}(\rho, \varphi, z_c; t) d\rho, \tag{36}$$

and then the maximum value of  $\overline{\mathcal{L}}(\varphi, z_c; t)$  and the related value of  $\varphi$ , referred to as  $\varphi^*$ , are determined

$$\overline{\mathcal{L}}_{max}(z_c; t) = \overline{\mathcal{L}}(\varphi^*, z_c; t) = \max_{\varphi} \overline{\mathcal{L}}(\varphi, z_c; t) \tag{37}$$

The corresponding evolutions of  $\overline{\mathcal{L}}_{max}$  and its position of occurrence  $\varphi^*$  are documented in Fig. 13 (for the more realistic interpolation option, interpolation strategy II in Section 3.2). A very high utilization degree at MP1 (in the crown) is experienced right after the installation of the top heading on Dec 15 (corresponding to large compressive forces in the crown, see Fig. 12). When the tunnel is driven on, the forces re-distribute into the rock surrounding MC1452, so that the maximum utilization degree reduces, and continuously moves towards MP2 being positioned at the interface of the top heading and the left bench (where the bench excavation is expected first). Bench excavation leads to again larger utilization degree, alternating between the left-hand and right-hand end of the top heading, but never reaching

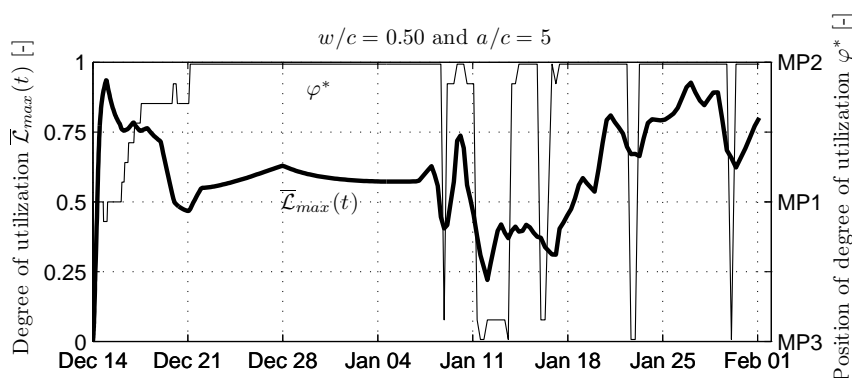


Figure 13: History of degree of utilization and its position for MC1452 of Sieberg tunnel using interpolation strategy II

the crown again (see Fig. 13). It is interesting to relate the aforementioned utilization degrees to the governing stress resultants, namely (compressive) normal forces in the circumferential and longitudinal directions, see Fig. 14. Thereby,  $n_z$  follows from definition (34), when replacing  $\varphi$  by  $z$ . As a rule, the longitudinal normal forces are smaller than the circumferential normal forces, but they are of a comparable order of magnitude. The highest compressive forces first occur in the crown, and afterwards move towards the left side of the tunnel, while the right-hand end of the top heading remains virtually free of (compressive) normal forces. Upon bench excavation, the crown does not undergo any (compressive) normal force loading, while the two ends of the (now well hydrated and stiffened) top heading undergo considerable normal forces, reaching magnitudes marking the absolute maximum encountered in MC1452 during the one and a half months of its existence.

## 8 Conclusion

Interpolation of polar components of point-wisely measured displacement vectors, in combination with thin shell theory and micromechanical modeling of shotcrete, allows for realistically estimating the loading states in shotcrete tunnel shells, at an unprecedented computational efficiency, rendering the diffusion of the proposed tool into tunnel engineering practice as very probable. In particular, the potential of micromechanics-driven explicit consideration of different shotcrete mixture characteristics (and of understanding their effects on the overall tunnel behavior) might open a new generation of shotcrete performance-based monitoring tools in geotechnical engineering.

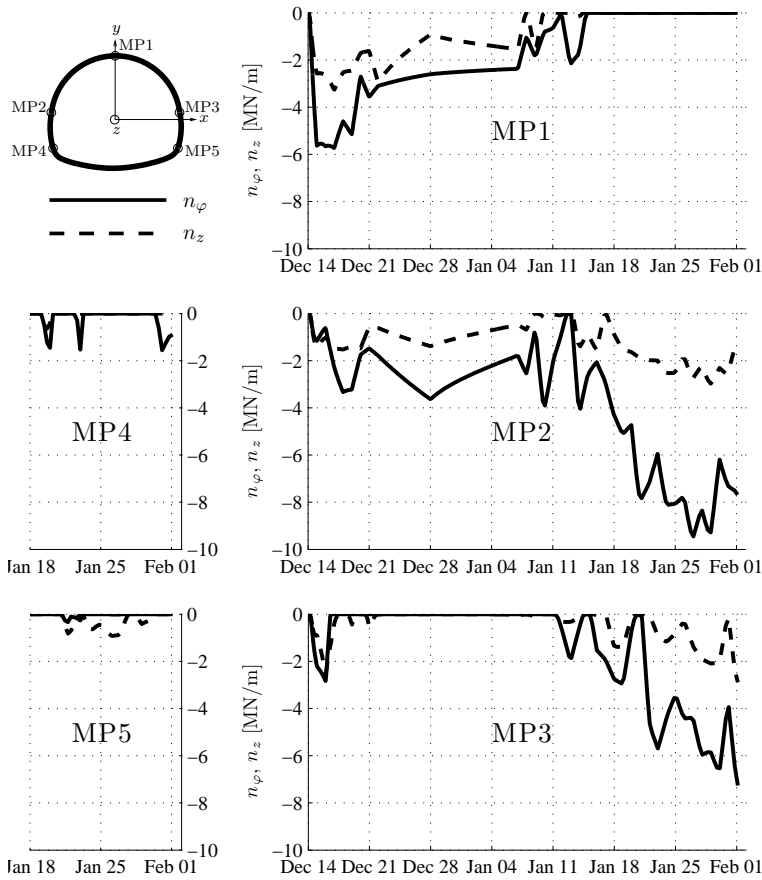


Figure 14: Evolution of circumferential and longitudinal normal forces acting at measurement points MP1 through MP5 of the *considered* measurement cross-section (MC1452) of the Sieberg tunnel

**Acknowledgement:** The first author gratefully acknowledges a scholarship granted by the Higher Education Commission (HEC) of Pakistan, enabling his doctoral studies at the Vienna University of Technology (TU Wien).

**List of symbols and abbreviations**

- $\underline{A}_\varphi, \underline{A}_z$  covariant in-plane base vectors of the *undeformed* reference surface
- $\underline{A}_r$  covariant out-of-plane base vector of the *undeformed* reference surface

$a, b$	coefficients of linear interpolation in longitudinal direction
$\underline{\underline{\underline{\mathbb{C}}}}_{sc}$	elastic stiffness tensor of shotcrete
$c, d, e$	coefficients of quadratic interpolation along top heading
$\underline{e}_x, \underline{e}_y, \underline{e}_z$	unit base vectors of fixed Cartesian coordinate system (with $x$ -, $y$ - and $z$ -axis)
$\underline{e}_r, \underline{e}_\varphi, \underline{e}_z$	unit base vectors of moving shell-intrinsic (cylindrical) coordinate system (with polar coordinates $r$ -, $\varphi$ - and $z$ )
$e_{ij}$	linearized strain tensor
$f, g$	coefficients of linear interpolation along left bench
$f_c$	uniaxial compressive strength of shotcrete
$f_b$	biaxial compressive strength of shotcrete
$\underline{G}_\varphi, \underline{G}_z$	covariant in-plane base vectors at a distance $\rho$ from the <i>undeformed</i> reference surface
$\underline{G}_r$	covariant out-of-plane base vector at a distance $\rho$ from the <i>undeformed</i> reference surface
$G_{ij}$	covariant components of the metric tensor at a distance $\rho$ from the <i>undeformed</i> reference surface
$\underline{g}_\varphi, \underline{g}_z$	covariant in-plane base vectors at a distance $\rho$ from the <i>deformed</i> reference surface
$\underline{g}_r$	covariant out-of-plane base vector at a distance $\rho$ from the <i>deformed</i> reference surface
$g_{ij}$	covariant components of the metric tensor at a distance $\rho$ from the <i>deformed</i> reference surface
$h$	thickness of shotcrete tunnel shell
$\underline{\underline{\underline{\mathbb{I}}}}$	symmetric fourth-order unity tensor
$\underline{\underline{\mathbb{1}}}$	second-order unity tensor
$\underline{\underline{\mathbb{J}}}$	volumetric part of the symmetric fourth-order unity tensor
$\underline{\underline{\underline{\mathbb{J}}}}$	macroscopic fourth-order creep tensor
$\underline{\underline{\underline{\mathbb{K}}}}$	deviatoric part of the symmetric fourth-order unity tensor
$k_{sc}$	elastic bulk modulus of shotcrete
$k_c$	creep bulk modulus of shotcrete
$k_{DP}$	strength-like quantity in Drucker-Prager failure criterion
$\mathcal{L}$	level of loading (utilization degree)
$\overline{\mathcal{L}}$	utilization degree averaged over tunnel shell thickness
$\overline{\mathcal{L}}_{max}$	maximum of $\mathcal{L}$ within one cross-section
MC	measurement cross-section

MCc	<i>considered</i> measurement cross-section
MCp	<i>preceding</i> measurement cross-section
MP	measurement point
MPk	k-th measurement point
$m_\varphi$	circumferential bending moment per unit length of the tunnel shell
$n_\varphi$	circumferential normal force per unit length of the tunnel shell
$q$	scalar quantity (defining displacement components)
$R$	radius of the <i>undeformed</i> reference surface
$r$	radial coordinate (in cylindrical coordinate system)
$R_b$	radius of midsurface of the tunnel benches
$R_t$	radius of midsurface of the tunnel top heading
$s$	radial coordinate with origin at the midsurface
$\underline{\underline{s}}$	second-order tensor of stress deviator
$t$	time variable
$\Delta t$	time increment
$t_{4,0}^c$	time of installation of MP4 (left bench) at the <i>considered</i> MC
$t_{5,0}^c$	time of installation of MP5 (right bench) at the <i>considered</i> MC
$t_{k,0}^c$	time of installation of MPk at <i>considered</i> MC
$t_{k,0}^p$	time of installation of MPk at <i>preceding</i> MC
$\underline{u}$	displacement vector
$u_x, u_y, u_z$	displacement components in Cartesian coordinate system (with x-, y- and z-axis)
$u_r, u_\varphi, u_z$	displacement components in cylindrical coordinate system (with polar coordinates $r, \varphi, z$ )
$\underline{X}$	position vector of a point on the <i>undeformed</i> reference surface
$\underline{x}$	position vector of a point on the <i>deformed</i> reference surface
$z$	longitudinal coordinate
$z_c$	position of <i>considered</i> MC along z-axis
$z_p$	position of <i>preceding</i> MC along z-axis
$\alpha$	index referring to circumferential and to axial directions, respectively
$\alpha_T$	thermal expansion coefficient of shotcrete
$\alpha_{DP}$	dimensionless parameter of Drucker-Prager failure criterion
$\underline{\underline{\varepsilon}}$	second-order tensor of total strains
$\varepsilon_h$	uniaxial yield strain of steel
$\underline{\underline{\varepsilon}}_T$	second-order tensor of thermal strains
$\underline{\underline{\varepsilon}}_M$	second-order tensor of mechanical strains
$\eta$	affine creep rate scaling function - ratio of nonlinear to linear creep
$\mu_{sc}$	elastic shear modulus of shotcrete

$\mu_c$	creep shear modulus of shotcrete
$\xi$	hydration degree of shotcrete
$\kappa$	ratio of biaxial to uniaxial compressive strength of shotcrete
$\rho$	radial distance of a point from the reference surface
$\tau$	time instant of loading in a classical creep test
$\underline{\underline{\sigma}}$	second-order stress tensor
$\underline{\underline{\Delta\sigma}}$	increment of second-order stress tensor
$\varphi^*$	position of maximum degree of utilization $\overline{\mathcal{L}}_{max}$
$+\varphi_{tb} = \varphi_2$	polar angle of the interface between the top heading and the left bench (MP2)
$-\varphi_{tb} = \varphi_3$	polar angle of the interface between the top heading and the right bench (MP3)
$+\varphi_{bi} = \varphi_4$	polar angle of the interface between the left bench and the invert (MP4)
$-\varphi_{bi} = \varphi_5$	polar angle of the interface between the right bench and the invert (MP5)
$\wedge$	exterior product (cross product) of two vectors in 3D Euclidean space
$\cdot$	inner product of two vectors in 3D Euclidean space
$:$	second-order tensor contraction

## References

- Acker, P.** (2001): Micromechanical analysis of creep and shrinkage mechanisms. In *Ulm, F.-J., Bažant, Z.P. and Wittmann, F.H. (eds) Concreep 6: Creep, Shrinkage and Durability of Concrete and Concrete Structures, Cambridge, USA*, pp. 15–25. Elsevier Science Ltd.
- Acker, P.; Fourier, C.; Malier, Y.** (1986): Temperature related mechanical effects in concrete elements and optimization in the manufacturing process. In *Young F. editor, Concrete at early ages*, pp. 33–48. American Concrete Institute, Detroit, Michigan, USA.
- Basar, Y.; Krätzig, W.** (2001): *Theory of Shell Structures*. Fortschritt-Berichte VDI, Reihe 18, Nr. 258. Ruhr-Universität Bochum.
- Bilaniuk, N.; Wong, G. S. K.** (1993): Speed of sound in pure water as a function of temperature. *Journal of the Acoustical Society of America*, vol. 93, no. 3, pp. 1609–1612.
- Böhm, H. J.; Han, W.; Eckschlager, A.** (2004): Multi-inclusion unit cell studies of reinforcement stresses and particle failure in discontinuously reinforced ductile

matrix composites. *CMES: Computer Modeling in Engineering and Sciences*, vol. 5, no. 1, pp. 5–20.

**Byfors, J.** (1980): *Plain concrete at early ages*. Swedish Cement and Concrete Research Institute. Stockholm, Sweden.

**CEB-FIP** (1990): *Model Code for Concrete Structures*. Comité Euro-International Du Béton and International Federation for Prestressing. Thomas Telford.

**Cirak, F.; Ortiz, M.; Schröder, P.** (2000): Subdivision surfaces: a new paradigm for thin-shell Finite-Element Analysis. *International Journal for Numerical Methods in Engineering*, vol. 47, no. 12, pp. 2039–2072.

**Fung, Y.** (1965): *Foundations of Solid Mechanics*. Prentice-Hall international series in dynamics. Prentice Hall.

**Hellmich, C.** (1999): *Shotcrete as part of the New Austrian Tunneling Method: From Thermochemomechanical Material Modeling to Structural Analysis and Safety Assessment of Tunnels*. PhD thesis, Vienna University of Technology, Vienna, Austria, 1999.

**Hellmich, C.; Macht, J.; Mang, H.** (1999): Ein hybrides Verfahren zur Bestimmung der Auslastung von Spritzbetonschalen auf der Basis von in-situ Verschiebungsmessungen und thermochemomechanischer Materialmodellierung [A hybrid method for determination of the degree of utilization of shotcrete tunnel linings on the basis of in-situ displacement measurements and thermochemomechanical material modeling] (in German). *Felsbau*, vol. 17, no. 5, pp. 422–425.

**Hellmich, C.; Mang, H.** (1999): Influence of the dilatation of soil and shotcrete on the load bearing behavior of NATM-Tunnels. *Felsbau*, vol. 17, no. 1, pp. 35–43.

**Hellmich, C.; Mang, H.** (2005): Shotcrete elasticity revisited in the framework of continuum micromechanics: from submicron to meter level. *Journal of Materials in Civil Engineering (ASCE)*, vol. 17, no. 3, pp. 246–256.

**Hellmich, C.; Mang, H.; Ulm, F.-J.** (2001): Hybrid method for quantification of stress states in shotcrete tunnel shells: combination of 3D in situ displacement measurements and thermochemoplastic material law. *Computers and Structures*, vol. 79, no. 22–25, pp. 2103–2115.

**Hellmich, C.; Ulm, F.-J.; Mang, H.** (1999): Consistent linearization in Finite Element analysis of coupled chemo-thermal problems with exo- or endothermal reactions. *Computational Mechanics*, vol. 24, pp. 238–244.

**Hofstetter, G.; Simo, J.; Taylor, R.** (1993): A modified cap model: Closest point solution algorithms. *Computers and Structures*, vol. 46, no. 2, pp. 203–214.

**Huang, L.; Xu, Z.; Zhou, C.** (2009): Modeling and monitoring in a soft argillaceous shale tunnel. *Acta Geotechnica*, vol. 4, pp. 273–282.

**Knauss, W.** (2003): Viscoelasticity and the time-dependent fracture of polymers. *Comprehensive Structural Integrity*, vol. 2, no. 7, pp. 383–428.

**Koiter, W. T.; Simmonds, J.** (1972): Foundation of Shell Theory. In *Sectional lecture presented at the 13th International Congress of Theoretical and Applied Mechanics. Masco, August 21-26, 1972*. Department of Mechanical Engineering, Delft University of Technology, The Netherlands.

**Lackner, R.; Macht, J.; Hellmich, C.; Mang, H.** (2002): Hybrid method for analysis of segmented shotcrete tunnel linings. *Journal of Geotechnical and Geoenvironmental Engineering (ASCE)*, vol. 128, no. 4, pp. 298–308.

**Lackner, R.; Macht, J.; Mang, H.** (2006): Hybrid analysis method for on-line quantification of stress states in tunnel shells. *Computer Methods in Applied Mechanics and Engineering*, vol. 195, no. 41–43, pp. 5361–5378.

**Laplante, P.** (1993): *Propriétés mécaniques de bétones durcissants: Analyse comparée des bétons classique et à très hautes performances (Mechanical properties of hardening concrete: A comparative analysis of ordinary and high performance concretes) (in French)*. PhD thesis, Ecole Nationale des Ponts et Chaussées, Paris, France, 1993.

**Love, A.** (1944): *A Treatise on the Mathematical Theory of Elasticity*. Dover Publications Inc.

**Macht, J.; Lackner, R.; Hellmich, C.; Mang, H.** (2003): Quantification of stress states in shotcrete shells. In *Beer G (ed.) Numerical Simulation in Tunneling*, pp. 225–248. Springer-Verlag Wien New York.

**Maidl, B.; Schmid, L.; Ritz, W.; Herrenknecht, M.** (2008): *Hardrock Tunnel Boring Machines*. Ernst and Sohn.

**Meschke, G.** (1996): Consideration of aging of shotcrete in the context of a 3-D viscoplastic material model. *International Journal for Numerical Methods in Engineering*, vol. 39, no. 18, pp. 3123 – 3143.

**Möller, S. C.; Vermeer, P. A.** (2008): On numerical simulation of tunnel installation. *Tunnelling and Underground Space Technology*, vol. 23, pp. 461 – 475.

**Oettl, G.; Stark, R. F.; Hofstetter, G.** (1998): A comparison of elastic-plastic soil models for 2D FE analyses of tunnelling. *Computers and Geotechnics*, vol. 23, pp. 19 – 38.

- Okada, H.; Fukui, Y.; Kumazawa, N.** (2004): Homogenization analysis for particulate composite materials using the boundary element method. *CMES: Computer Modeling in Engineering and Sciences*, vol. 5, no. 2, pp. 135–149.
- Pacher, F.** (1964): Deformationsmessungen im Versuchsstollen als Mittel zur Erforschung des Gebirgsverhaltens und zur Bemessung des Ausbaus [Measurements of deformations in experimental tunnels to explore the behavior of rock and to design the lining] (in German). *Felsmechanik und Ingenieurgeologie*, vol. I, pp. 149 – 161.
- Pellet, F. L.** (2009): Contact between a tunnel lining and a damage-susceptible viscoplastic medium. *CMES: Computer Modeling in Engineering and Sciences*, vol. 52, no. 3, pp. 279–295.
- Pichler, B.; Hellmich, C.; Eberhardsteiner, J.** (2009): Spherical and acicular representation of hydrates in a micromechanical model for cement paste: prediction of early-age elasticity and strength. *Acta Mechanica*, vol. 203, no. 3-4, pp. 137 – 162.
- Pichler, B.; Scheiner, S.; Hellmich, C.** (2008): From micron-sized needle-shaped hydrates to meter-sized shotcrete tunnel shells: micromechanical upscaling of stiffness and strength of hydrating shotcrete. *Acta Geotechnica*, vol. 3, no. 4, pp. 273 – 294.
- Poleschinski, V. W.; Müller, P.** (1999): Geologische Dokumentation des Siebergtunnels und der Voreinschnitte [Geological documentation of Sieberg tunnel and the Open Cuts] (in German). *Felsbau*, vol. 17, no. 2, pp. 112 – 119.
- Powers, T.; Brownyard, T.** (1948): Studies of the physical properties of hardened portland cement paste. *Research Laboratories of the Portland Cement Association Bulletin*, vol. 22, pp. 101 – 992.
- Pyo, S. H.; Lee, H. K.** (2009): Micromechanical analysis of aligned and randomly oriented whisker-/ short fiber-reinforced composites. *CMES: Computer Modeling in Engineering and Sciences*, vol. 40, no. 3, pp. 271–305.
- Rabcewicz, L.** (1948): Patentschrift: Österreichisches Patent Nr. 165573 (Patent specification: Austrian patent no. 165573) [in German], 1948.
- Rabcewicz, L.** (1969): Stability of tunnels under rock load, Part I, Part II, and Part III. *Water Power*, pp. 225–229, 266–273, and 297–302.
- Ramsbacher, V. W.; Schwab, P.** (1998): Siebergtunnel, Vortrieb Pillgrab West – Planung und Ausführung [Driving of Sieberg tunnel towards west - planning and execution] (in German). *Österreichische Ingenieur und Architekten-Zeitschrift (ÖIAZ)*, vol. 9, pp. 302–305.

**Rettighieri, M.; Triclot, J.; Mathieu, E.; Berla, G.; Panet, M.** (2008): Difficulties associated with high convergences during excavation of the Saint Martin La Porte access adit. In *Proceedings of the International Congress, Building Underground for the Future*, pp. 395–403. AFTES, Monaco.

**Rokahr, R.** (1997): Ein neues Verfahren zur täglichen Kontrolle der Auslastung einer Spritzbetonschale [A new method for daily monitoring of the stress intensity of a shotcrete lining] (in German). *Felsbau*, vol. 15, no. 6, pp. 430–434.

**Ruiz, M.; Muttoni, A.; Gambarova, P.** (2007): Relationship between nonlinear creep and cracking of concrete under uniaxial compression. *Journal of Applied Concrete Technology*, vol. 5, no. 3, pp. 383–393.

**Sanahuja, J.; Dormieux, L.; Meille, S.; Hellmich, C.; Fritsch, A.** (2010): Micromechanical explanation of elasticity and strength of gypsum: From elongated anisotropic crystals to isotropic porous polycrystals. *Journal of Engineering Mechanics (ASCE)*, vol. 136, no. 2, pp. 239–253.

**Sandler, I. S.; Rubin, D.** (1979): An algorithm and a modular subroutine for the cap model. *International Journal for Numerical and Analytical Methods in Geomechanics*, vol. 3, pp. 173–176.

**Scheiner, S.; Hellmich, C.** (2009): Continuum microviscoelasticity model for aging basic creep of early-age concrete. *Journal of Engineering Mechanics (ASCE)*, vol. 135, no. 4, pp. 307–323.

**Schubert, W.; Steindorfer, A.** (1996): Selective displacement monitoring during tunnel excavation. *Felsbau*, vol. 14, no. 2, pp. 93–97.

**Smith, D.; Booker, J.** (1996): Boundary element analysis of linear thermoelastic consolidation. *International Journal for Numerical and Analytical Methods in Geomechanics*, vol. 20, pp. 457–488.

**Städling, A.; Winselmann, D.** (1998): Beanspruchungen des zweischaligen Tunnelausbaus unter Berücksichtigung des Baufortschrittes [Stresses in the outer and inner tunnel lining under consideration of construction phases] (in German). *Bauingenieur*, vol. 73, no. 5, pp. 215–219.

**Steindorfer, A.; Schubert, W.** (1997): Application of new methods of monitoring data analysis for short term prediction in tunnelling. In *Golser J., Hinkel W.J. and Schubert W. (editors), Tunnels for People, Proceedings of the World Tunnel Congress*, volume 1, pp. 9–65. Balkema, Rotterdam, The Netherlands.

**Steindorfer, A.; Schubert, W.; Rabensteiner, K.** (1995): Problemorientierte Auswertung geotechnischer Messungen [Advanced analysis of geotechnical displacement monitoring data: new tools and examples of application] (in German). *Felsbau*, vol. 13, no. 6, pp. 386–390.

**Ulm, F.-J.; Constantinides, G.; Heukamp, F.** (2004): Is concrete a poromechanics material? – A multiscale investigation of poroelastic properties. *Materials and Structures / Concrete Science and Engineering*, vol. 37, no. 1, pp. 43–58.

**Ulm, F.-J.; Coussy, O.** (1996): Strength growth as chemo-plastic hardening in early age concrete. *Journal of Engineering Mechanics (ASCE)*, vol. 122, no. 12, pp. 1123–1132.

**Weissbach, V. G.; Juli, R.** (1984): Finite Elemente Berechnung eines Lehnentunnels unter Berücksichtigung des Trennflächensystems im Gebirge [Finite Element computation of a tunnel in a mountain slope, under consideration of rock faults] (in German). *H. Grundmann, E. Stein, W. Wunderlich, editors, Finite Elemente in der Baupraxis*, pp. 377–387.

**Zaoui, A.** (2002): Continuum micromechanics: survey. *Journal of Engineering Mechanics (ASCE)*, vol. 128, no. 8, pp. 808–816.

